



Numerical simulation of propagation problems on the sphere with a compact scheme

Matthieu Brachet, Jean-Pierre Croisille

► To cite this version:

Matthieu Brachet, Jean-Pierre Croisille. Numerical simulation of propagation problems on the sphere with a compact scheme. Computers and Fluids, 2022. hal-01803633v2

HAL Id: hal-01803633

<https://hal.science/hal-01803633v2>

Submitted on 2 Jul 2019

HAL is a multi-disciplinary open access archive for the deposit and dissemination of scientific research documents, whether they are published or not. The documents may come from teaching and research institutions in France or abroad, or from public or private research centers.

L'archive ouverte pluridisciplinaire **HAL**, est destinée au dépôt et à la diffusion de documents scientifiques de niveau recherche, publiés ou non, émanant des établissements d'enseignement et de recherche français ou étrangers, des laboratoires publics ou privés.

A CENTER COMPACT SCHEME FOR THE SHALLOW WATER EQUATIONS ON THE SPHERE

M. BRACHET[†] AND J.-P. CROISILLE[‡]

ABSTRACT. We consider the Shallow Water Equations (SWE) on a rotating sphere and their approximation by a finite difference scheme. The discrete unknowns are located at the vertices of the equiangular Cubed Sphere grid, [11, 12]. The standard fourth order Hermitian difference derivative [24] is used along a set of suitable great circles. No one sided difference formula is used at any point. All differential operators on the sphere (gradient, divergence and curl) are approximated in a centered fashion. The approximation procedure is close in spirit to the one of compact schemes used in Computational Aeroacoustics. Numerical results on a series of numerical test cases for SWE on the sphere are presented. A particular attention is devoted to the temporal scheme. In particular two Rosenbrock exponential time schemes are used and compared to the RK4 scheme.

The results demonstrate the interest of the present approach in a variety of situations of interest in numerical climatology.

Keywords: Cubed Sphere grid - Compact finite difference scheme - Hermitian derivative - Rosenbrock time scheme - Spherical Shallow Water equations

1. INTRODUCTION

In this paper a new finite difference scheme for the Shallow Water Equations (SWE) on the rotating sphere is considered. The SWE equations represent the basic propagation system of interest in numerical climatology at global scale, [17, 26]. This system is routinely solved by spectral methods [23] with models of various complexity (single or multilayer, hydrostatic or nonhydrostatic, etc.). Over the past twenty years, many efforts have been devoted to renew numerical schemes for Global Circulation Models (GCM) by adapting ideas from Computational Fluid Dynamics (CFD) to Geophysical Fluid Dynamics (GFD). Solving (SWE) in the two dimensional spherical setup was a first step in this direction. To assess the accuracy of the numerical methods, several series of test cases have been suggested, [7, 14, 45].

Conservative approximation frameworks have been considered as a suitable platform to develop new methods for GCM. A natural option is the finite volume method. It can be considered on various kinds of grids in [4, 8, 35]. The Discontinuous Galerkin method is also considered in [2]. Another possibility is the spectral element method. It is explored and analyzed in [18, 19]. Another point of view recently developed in [13, 39] is the one of discrete differential topology and the associated Mimetic Finite Element (or Finite Volume) framework. In all these methods, referred to as the conservative approach, there is a primal grid supporting discrete averages. Numerical degrees of freedom are attached to this primal grid or alternatively to a second grid in dual position with the primal grid. In the conservative approach, discrete conservation holds *ab initio*, at least for the mass.

In the present work, we do not start from a discrete flux form of (SWE). Instead we consider a direct finite difference approximation. The equiangular Cubed Sphere is used as the sole grid. All the discrete unknowns are located at the vertices of the Cubed Sphere in a finite difference fashion. There is no staggered nor mean value variables in the cells of the Cubed Sphere. A center compact formula is then applied at each vertex of the Cubed Sphere to calculate approximate derivatives. The geometric structure of the Cubed Sphere plays a central role in our approximation. This approach is directly inspired by high order finite differencing in Computational Aeroacoustics (CAA) [5, 24]. In CAA, the main goal is to ensure an accurate numerical

Date: June 30 2019.

The first author thanks L. Debreux and C. Eldred for fruitful discussions. Most of this work has been performed during the doctoral thesis of the first author at the Inst. Elie Cartan de Lorraine, and the mathematics department of the U. de Lorraine (Metz).

propagation of linear waves or of weakly nonlinear waves. This is also a central objective in Geophysical Fluid Dynamics: linear waves related to SWE must be numerically advected over long physical intervals of time. Therefore a numerical scheme based on the same premises than compact schemes in CAA seems highly desirable, also in the GFD context.

Our finite difference approximation follows the principles introduced in [11, 12]. The basic idea is to use high order differencing along a set of great circles suitably associated to the structure of the equiangular Cubed Sphere. This great circles approach permits to handle the full sphere with the same periodic treatment. Doing so, there is no need of any one sided difference formulas to handle interpanel boundaries. This has been proved to be of great importance to preserve the accuracy over a large number of time iterations.

Compact formulas for the derivatives are commonly centered formulas. Enhancing stability is obtained by adding some numerical dissipation. A typical practice in CAA is to add a high frequency filtering at each time step. In our approach, performing such a filtering step has been found efficient as well.

The objective and the summary of this paper are as follows. In Section 2, we recall the background of our centered differencing along great circles on the Cubed Sphere [11, 12]. The three operators that are approximated are grad_T , div_T and curl_T also denoted as ∇_T , $\nabla_T \cdot$ and $\nabla_T \times$, respectively. In the three cases, the approximation principle is similar.

In Section 3, the two time stepping used in our simulations are described. First, the explicit RK4 scheme is our reference time scheme. A CFL condition must be used with this scheme. Our second time stepping consists of two exponential schemes belonging to the Rosenbrock family. They have been compared with the RK4 scheme.

In Section 4, numerical results for (SWE) are shown for the isolated mountain, the Rossby-Haurwitz and the barotropic instability test cases. In each case, we show that our scheme compares favourably with high order conservative upwind methods, such as [2, 25, 41]. The accuracy is well preserved over a large number of time steps. In addition, all conserved quantities at the continuous level are as well remarkably well preserved at the discrete level. This includes the mass, the total energy, and the potential enstrophy. The meaning of this conservation is related to the quadrature formula on the Cubed Sphere in [29].

All the computations were performed in *Matlab* on a desktop computer.

2. A CENTER SCHEME FOR THE SHALLOW WATER EQUATIONS ON THE CUBED SPHERE

Let \mathbb{S}_a be the sphere of radius a , ($a = 6371$ km for the earth). The Shallow Water Equations let evolve the height and (tangent) wind velocity $(t, \mathbf{x}) \in [0, +\infty[\times \mathbb{S}_a \mapsto (h(t, \mathbf{x}), \mathbf{u}(t, \mathbf{x}))$ by (g is the gravity constant),

$$(1) \quad (SWE) \quad \begin{cases} \frac{\partial h^*}{\partial t}(t, \mathbf{x}) + \nabla_T \cdot (h^*(t, \mathbf{x}) \mathbf{u}(t, \mathbf{x})) = 0 \\ \frac{\partial \mathbf{u}}{\partial t}(t, \mathbf{x}) + \nabla_T \left(\frac{1}{2} |\mathbf{u}(t, \mathbf{x})|^2 + gh(t, \mathbf{x}) \right) + \left(f(\mathbf{x}) + \zeta(\mathbf{x}, \mathbf{u}(t, \mathbf{x})) \right) \mathbf{n}(\mathbf{x}) \times \mathbf{u}(t, \mathbf{x}) = \mathbf{0} \end{cases}$$

This is the *vector form* of the Shallow Water Equation, [45]. The three given functions in (SWE) are

$$(2) \quad \begin{cases} \mathbf{x} \in \mathbb{S}_a \mapsto \mathbf{n}(\mathbf{x}) \in \mathbb{T}\mathbb{S}_a^\perp, \text{ exterior normal} \\ \mathbf{x} \in \mathbb{S}_a \mapsto f(\mathbf{x}) \in \mathbb{R}, \text{ Coriolis force} \\ \mathbf{x} \in \mathbb{S}_a \mapsto h_s(\mathbf{x}) \in \mathbb{R}_+, \text{ bottom topography.} \end{cases}$$

The *relative vorticity* $\zeta(\mathbf{x}, \mathbf{v}(\mathbf{x}))$ associated with the velocity field $\mathbf{v}(\mathbf{x})$ is the function defined by

$$(3) \quad \zeta(\mathbf{x}, \mathbf{v}(\mathbf{x})) = (\nabla_T \times \mathbf{v}(\mathbf{x})) \cdot \mathbf{n}(\mathbf{x}).$$

The *total height* of the atmosphere is

$$(4) \quad h^*(t, \mathbf{x}) = h(t, \mathbf{x}) - h_s(\mathbf{x}).$$

Denoting $(t, \mathbf{x}) \in [0, +\infty[\times \mathbb{S}_a^2 \mapsto \mathbf{q}(t, \mathbf{x}) = [h(t, \mathbf{x}), \mathbf{u}(t, \mathbf{x})]^T \in \mathbb{R}^4$, (1) is expressed as

$$(5) \quad \frac{\partial}{\partial t} \mathbf{q}(t, \mathbf{x}) = J(\mathbf{x}, \mathbf{q}(t, \mathbf{x})),$$

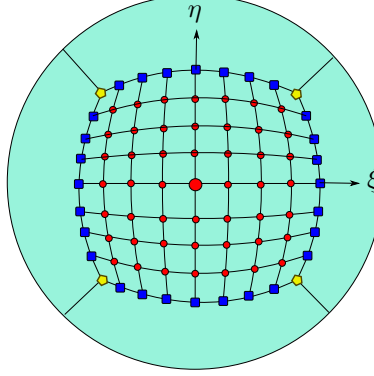


FIGURE 1. Frontal view of a panel of the Cubed Sphere $\mathbb{CS}_{a,N}$. The vertices are classified in three categories: (i) $(N-1)^2$ internal vertices displayed with circles; (ii) $4(N-1)$ edge vertices displayed with squares; (iii) 4 corner vertices displayed with pentagons. The equatorial angles (ξ, η) (local coordinates) are such that $-\pi/4 \leq \xi, \eta \leq \pi/4$, with origin at the center of the panel. The vertices in panel k are denoted $\mathbf{s}_{i,j}^k$. The integer i (resp. j) denotes the index in the ξ direction (resp. η) direction. A gridfunction defined on $\mathbb{CS}_{a,N}$ consists of $6N^2 + 2$ data located at $\mathbf{s}_{i,j}^k$ $-N/2 \leq i, j \leq N/2$ and $(I) \leq k \leq (VI)$. The spatial steps are identical in the ξ and η directions with resolution $\Delta_N = \Delta\xi = \Delta\eta = \frac{\pi}{2N}$.

with

$$(6) \quad J(\mathbf{x}, \mathbf{q}(\mathbf{x})) = - \left(\begin{array}{c} \nabla_T \cdot ((h(\mathbf{x}) - h_s(\mathbf{x}))\mathbf{u}(\mathbf{x})) \\ \nabla_T \left(\frac{1}{2} |\mathbf{u}(\mathbf{x})|^2 + g h(t, \mathbf{x}) \right) + (f(\mathbf{x}) + \zeta(\mathbf{x}, \mathbf{u}(\mathbf{x})) \mathbf{n}(\mathbf{x}) \times \mathbf{u}(\mathbf{x})) \end{array} \right).$$

The notation $\mathbb{CS}_{a,N}$ stands for the *equiangular Cubed Sphere* grid with radius a and parameter N .¹ We consider on \mathbb{S}_a the six panels $k = (I), \dots, (VI)$ matching the faces of a cube. A typical panel is represented in Fig. 1. The local chart of each panel is the system of angles $(\xi, \eta) \in [-\pi/2, \pi/2] \times [-\pi/2, \pi/2]$. Each panel contains a set of vertices defined by $\mathbf{s} = [\mathbf{s}_{i,j}^k]$, $-N/2 \leq i, j \leq N/2$, $(I) \leq k \leq (VI)$ with local coordinates $\xi_i = i\Delta_N$, $\eta_j = j\Delta_N$. The step size is $\Delta_N = \Delta\xi = \Delta\eta = \pi/2N$.

Proceeding along the method of lines, (1) is first approximated in space by the semi-discrete system

$$(7) \quad \frac{d}{dt} \mathbf{q}(t) = J_{\Delta_N}(\mathbf{s}, \mathbf{q}(t)).$$

The semidiscrete function $\mathbf{q}(t)$ ² is $\mathbf{q}(t) = [\mathbf{h}(t), \mathbf{u}(t)]^T$ where

$$(8) \quad \mathbf{h}(t) = [h_{i,j}^k(t)]^T, \quad \mathbf{u}(t) = [\mathbf{u}_{i,j}^k(t)]^T, \quad -N/2 \leq i, j \leq N/2, k \in \{(I), \dots, (VI)\}.$$

For \mathbf{f}, \mathbf{g} , two given (scalar or vector) gridfunctions, the gridfunction $\{\mathbf{f} \bullet \mathbf{g}\}$ is defined by

$$(9) \quad \{\mathbf{f} \bullet \mathbf{g}\}_{i,j}^k = f_{i,j}^k g_{i,j}^k, \quad -N/2 \leq i, j \leq N/2, k \in \{(I), \dots, (VI)\}.$$

In the case of vector gridfunctions, one has $\{\mathbf{f} \bullet \mathbf{g}\}_{i,j}^k = \mathbf{f}_{i,j}^k \cdot \mathbf{g}_{i,j}^k$. Similarly $\{\mathbf{f} \times \mathbf{g}\}_{i,j}^k = \mathbf{f}_{i,j}^k \times \mathbf{g}_{i,j}^k$. The approximation of J on $\mathbb{CS}_{a,N}$ is J_{Δ_N} defined by

$$(10) \quad J_{\Delta_N}(\mathbf{s}, \mathbf{q}) = - \left(\begin{array}{c} \nabla_{T,\Delta_N} (\mathbf{h} - \{h_s(\mathbf{s}) \bullet \mathbf{u}\}) \\ \nabla_{T,\Delta_N} \left(\frac{1}{2} \{\mathbf{u} \bullet \mathbf{u}\} + g\mathbf{h} \right) + \{ (f(\mathbf{s}) + \zeta_{\Delta_N}) \bullet (\mathbf{n}(\mathbf{s}) \times \mathbf{u}) \} \end{array} \right)$$

¹Refer to [30] for different Cubed Sphere grids.

²We adopt the fraktur font for gridfunctions, i.e. functions defined at the vertices of $\mathbb{CS}_{a,N}$.

The gridfunction ζ_{Δ_N} is

$$(11) \quad \zeta_{\Delta_N} = (\nabla_{T,\Delta_N} \times \mathbf{u}) \bullet \mathbf{n}(\mathbf{s}).$$

In (10), the operators ∇_{T,Δ_N} , $\nabla_{T,\Delta_N} \cdot$ and $\nabla_{T,\Delta_N} \times$ are centered approximations of the operators ∇_T , div_T and curl_T , respectively. These approximations are defined as follows. Consider for example the discrete gradient ∇_{T,Δ_N} . Let $\mathbf{x} \in \mathbb{S}_a \mapsto f(\mathbf{x})$ be a given function. The value of f at the vertex $\mathbf{s}_{i,j}^k$ is $f_{i,j}^k = f(\mathbf{s}_{i,j}^k)$. Consider the panel (I) in Fig. 1. Fix an "horizontal" coordinate line (iso- η line $\eta = j_0 \Delta_N$). This coordinate line is a great circle section. Consider next the extension of this coordinate line to the full great circle around the sphere \mathbb{S}_a . On panel (III), opposite to panel (I), this great circle again matches an iso η coordinates line, this time with index $N - j_0$. On the contrary, on panels (II) and (IV), both adjacent to panel (I), this great circle does not coincide with any coordinate line. Next, define along this great circle a one dimensional grid associated with a set of data. On the panel (I) the grid coincides with the Cubed Sphere vertices $\mathbf{s}_{i,j_0}^{(I)}$. The data at these vertices are the values $f_{i,j_0}^{(I)}$. We proceed similarly on panel (III). On panel (II), the great circle intersects each "vertical" coordinates line $\xi = \xi_i$. This intersection defines a point to which some interpolated value, deduced from data in panel (II) is assigned. A similar procedure is performed on panel (IV). Summing up, this results in a grid of size $4N$ of the considered great circle with constant step size $\Delta\xi = \Delta_N$ and in a set of $4N$ periodic data along this circle. Then the finite difference $\delta_\xi^H f_p^k$, is applied to these data, using the relations

$$(12) \quad \frac{1}{6} \delta_\xi^H f_{p-1} + \frac{2}{3} \delta_\xi^H f_p + \frac{1}{6} \delta_\xi^H f_{p+1} = \frac{f_{p+1} - f_{p-1}}{2\Delta\xi}.$$

where the index $p = 1 \dots 4N$ stands for the index of the $4N$ periodic data along the great circle. The formal truncation error for $\delta_\xi^H f_p$ satisfies (assuming exact data at the gridpoints), [3]

$$(13) \quad \delta_\xi^H f_p - \partial_\xi f(\mathbf{s}_p^k) = O(\Delta_N^4).$$

Remark 2.1. The data on panels (II) and (IV) only serve as "ghost values". They permit to apply the periodic differencing (12) without taking care of any cut-off in panels (II) and (IV). After solving (12), only the finite difference values $\delta_\xi^H f$ located in panels (I) and (III) are retained and the values located in panels (II) and (IV) are discarded. We refer to [11, 12] for more details.

The computational procedure above is repeated for all the coordinate lines in the ξ direction for panels (I), (II) and (V); and similarly in the η direction for the same panels (I), (II) and (V). Due to the spherical symmetry, the couple of partial derivatives $(\partial_\xi f, \partial_\eta f)$ is approximated at each vertex of $\mathbb{CS}_{a,N}$. Note that this way to proceed ensures a perfect symmetry in the calculation.

Considering effective accuracy, according to (13), one may expect fourth order accurate for the approximate derivative. However, due to the interpolation of the data in panels (II) and (IV), the accuracy possibly could drop to 3. In fact, the value f_p assigned to point \mathbf{m}_p on the great circle satisfies

$$(14) \quad \begin{cases} f_p = f(\mathbf{m}_p) & \text{if } \mathbf{m} \text{ belongs to panels (I) or (III).} \\ f_p = f(\mathbf{m}_p) + O(\Delta_N^4) & \text{if } \mathbf{m} \text{ belongs to panels (II) or (IV).} \end{cases}.$$

Therefore it turns out that $(\Delta\xi = \Delta_N)$

$$(15) \quad \frac{f_{p+1} - f_{p-1}}{2\Delta\xi} = \frac{f(\mathbf{m}_{p+1}) - f(\mathbf{m}_{p-1})}{2\Delta\xi} + O(\Delta\xi^3),$$

which gives at the least

$$(16) \quad \delta_\xi^H f_p = \partial_\xi f(\mathbf{m}_p) + O(\Delta\xi^3).$$

In practice however, fourth order accuracy has been numerically observed so far. See also Section 4.6. The approximate gradient, divergence and curl are then calculated as follows. On the panel k , the local basis at the vertex $\mathbf{s}_{i,j}^k$ is $(\mathbf{g}_\xi, \mathbf{g}_\eta)$ given by

$$(17) \quad \mathbf{g}_\xi(\mathbf{s}_{i,j}^k) = \frac{\partial \mathbf{x}}{\partial \xi}(\mathbf{s}_{i,j}^k), \quad \mathbf{g}_\eta(\mathbf{s}_{i,j}^k) = \frac{\partial \mathbf{x}}{\partial \eta}(\mathbf{s}_{i,j}^k).$$

Refer to [11, 6] for the analytic expression of $(\mathbf{g}_\xi, \mathbf{g}_\eta)$. Let $\mathbf{x} \in \mathbb{S}_a \mapsto f(\mathbf{x})$ be a given function. We denote by f^* the restriction of f to the Cubed Sphere vertices:

$$(18) \quad (f^*)_{i,j}^k = f(\mathbf{s}_{i,j}^k).$$

The gradient of $f(\mathbf{x})$ is expressed at $\mathbf{s}_{i,j}^k$ in terms of the dual basis $(\mathbf{g}^\xi, \mathbf{g}^\eta)$ by

$$(19) \quad \nabla_T f(\mathbf{s}_{i,j}^k) = \frac{\partial f}{\partial \xi}(\mathbf{s}_{i,j}^k) \mathbf{g}^\xi(\mathbf{s}_{i,j}^k) + \frac{\partial f}{\partial \eta}(\mathbf{s}_{i,j}^k) \mathbf{g}^\eta(\mathbf{s}_{i,j}^k).$$

The partial derivatives $\frac{\partial f}{\partial \xi}(\mathbf{s}_{i,j}^k)$ and $\frac{\partial f}{\partial \eta}(\mathbf{s}_{i,j}^k)$ are approximated by the divided differences calculated by the above "great circle" procedure.

$$(20) \quad \frac{\partial f}{\partial \xi}(\mathbf{s}_{i,j}^k) \simeq \delta_\xi^H (f^*)_{i,j}^k, \quad \frac{\partial f}{\partial \eta}(\mathbf{s}_{i,j}^k) \simeq \delta_\eta^H (f^*)_{i,j}^k,$$

Similarly, consider a vector function $\mathbf{v}(\mathbf{x})$. The associated gridfunction is \mathbf{v}^* with components $(\mathbf{v}^*)_{i,j}^k = \mathbf{v}_{i,j}^k$. The divergence and curl operators are expressed in local coordinates as [36]

$$(21) \quad \begin{cases} \nabla_T \cdot \mathbf{v} = \partial_\xi \mathbf{v} \cdot \mathbf{g}^\xi + \partial_\eta \mathbf{v} \cdot \mathbf{g}^\eta, & (a) \\ \nabla_T \times \mathbf{v} = \mathbf{g}^\xi \times \partial_\xi \mathbf{v} + \mathbf{g}^\eta \times \partial_\eta \mathbf{v} & (b). \end{cases}$$

The partial derivatives $\partial_\xi \mathbf{v}$ and $\partial_\eta \mathbf{v}$ are approximated at $\mathbf{s}_{i,j}^k$ by

$$(22) \quad \partial_\xi \mathbf{v}(\mathbf{s}_{i,j}^k) \simeq \delta_\xi^H \mathbf{v}_{i,j}^k, \quad \partial_\eta \mathbf{v}(\mathbf{s}_{i,j}^k) \simeq \delta_\eta^H \mathbf{v}_{i,j}^k.$$

The approximations considered in the sequel to the gradient, the divergence and the curl, are the gridfunctions ∇_{T,Δ_N} , $\nabla_{T,\Delta_N} \cdot$ and $\nabla_{T,\Delta_N} \times$, with components

$$(23) \quad \begin{cases} (\nabla_{T,\Delta_N} f^*)_{i,j}^k = (\delta_\xi^H f^*)_{i,j}^k \mathbf{g}^\xi(\mathbf{s}_{i,j}^k) + (\delta_\eta^H f^*)_{i,j}^k \mathbf{g}^\eta(\mathbf{s}_{i,j}^k) & (a), \\ (\nabla_{T,\Delta_N} \cdot \mathbf{v}^*)_{i,j}^k = (\delta_\xi^H \mathbf{v}^*)_{i,j}^k \cdot \mathbf{g}^\xi(\mathbf{s}_{i,j}^k) + (\delta_\eta^H \mathbf{v}^*)_{i,j}^k \cdot \mathbf{g}^\eta(\mathbf{s}_{i,j}^k), & (b), \\ (\nabla_{T,\Delta_N} \times \mathbf{v}^*)_{i,j}^k = \mathbf{g}^\xi(\mathbf{s}_{i,j}^k) \times (\delta_\xi^H \mathbf{v}^*)_{i,j}^k + \mathbf{g}^\eta(\mathbf{s}_{i,j}^k) \times (\delta_\eta^H \mathbf{v}^*)_{i,j}^k & (c). \end{cases}$$

Remark 2.2. As mentioned in Remark 2.1, one may wonder if the redundancy in the "great circle" procedure could be avoided. For example, considering a small number of ghost points beyond the limit of a panel could give a smaller computational effort. In this spirit, the following alternative formula for the spherical divergence was suggested in [12], to which we refer for more details.

$$(24) \quad (\nabla_T \mathbf{v}^*)_{i,j}^k = \frac{1}{\sqrt{\det G}} \left(\partial_\xi \left(\sqrt{\det G} \mathbf{v}^* \cdot \mathbf{g}^\xi \right)_{i,j}^k + \partial_\eta \left(\sqrt{\det G} \mathbf{v}^* \cdot \mathbf{g}^\eta \right)_{i,j}^k \right).$$

We have adopted here (23)_b in order to have an homogeneous treatment of all differential terms in (SWE).

3. TIME DISCRETISATION

3.1. Basic setup. In Section 2, the spatial approximation of (1) was considered. Two kinds of time discretizations are used in Section 4. The reference time scheme is the standard RK4 scheme. The basic time marching algorithm is given in Algorithm 1.

Algorithm 1 : Explicit Runge-Kutta Scheme of order 4 with filter

```

1:  $\mathbf{q}^0 = \mathbf{q}^{(0)}$  given
2: for  $n = 0, 1, \dots, \text{itemax}$  do
3:    $K^{(1)} = J_{\Delta_N}(\mathbf{q}^n)$ ,
4:    $K^{(2)} = J_{\Delta_N}\left(\mathbf{q}^n + \frac{\Delta t}{2}K^{(1)}\right)$ ,
5:    $K^{(3)} = J_{\Delta_N}\left(\mathbf{q}^n + \frac{\Delta t}{2}K^{(2)}\right)$ ,
6:    $K^{(4)} = J_{\Delta_N}(\mathbf{q}^n + \Delta t K^{(3)})$ ,
7:    $\mathbf{q}^{n+1} = \mathcal{F}\left(\mathbf{q}^n + \frac{\Delta t}{6}(K^{(1)} + 2K^{(2)} + 2K^{(3)} + K^{(4)})\right)$ .
8: end for

```

In line 7, at the end of each time step a filtering step is applied. The function \mathcal{F} is the *filtering function*. As already mentioned, this filtering step is commonly used in CAA³ simulations. For details, refer to [5] and the references therein. The filter step enhances the stability of the scheme, but with accuracy preserving. The design of the filter function \mathcal{F} in one dimension is recalled in Section 6.3. In two dimensions, the filter function is obtained by tensor product. In the case of the Cubed Sphere $\mathbb{CS}_{a,N}$ we have used the following symmetric filter

$$(25) \quad \mathcal{F} = \frac{1}{2}(\mathcal{F}_\xi \circ \mathcal{F}_\eta + \mathcal{F}_\eta \circ \mathcal{F}_\xi),$$

where the functions \mathcal{F}_ξ and \mathcal{F}_η correspond to a 10-th order filter in the last line in Table 4 in Section 6.3. This choice has been proved to be a good compromise between accuracy and stability.

Remark 3.1. The filter function \mathcal{F}_ξ operates along the great circles as a periodic difference operator in a fashion similar to the difference operator δ_ξ^H ; and similarly for \mathcal{F}_η .

3.2. Two Rosenbrock time schemes. Beyond the RK4 time scheme mentioned above, we also have used two schemes of the Rosenbrock family [44, Ch. 7]. These schemes are particular examples of exponential time schemes. Recently, they have received interest for stiff problems as an alternative to implicit schemes. For flows over a sphere, refer to [9, 15]. With exponential time schemes, the stability constraint on the time step, related to the CFL condition in our case, is relaxed as when using an implicit time schemes. The damping of high frequency modes, which is a main goal of implicit time-stepping, is replaced with exponential schemes by the exact integration of the linear part of the source term. The design and convergence analysis of such schemes has been extensively documented. We refer to [22] for a recent review.

Consider the nonlinear differential system

$$(26) \quad \frac{d\mathbf{q}}{dt} = F(\mathbf{q}), \quad \mathbf{q}(0) = \mathbf{q}_0.$$

where $t \geq 0 \mapsto \mathbf{q}(t) \in \mathbb{R}^n$ is the semidiscrete vector in (7). The function $F : \mathbb{R}^n \mapsto \mathbb{R}^n$ represents the spatial discretisation in the RHS of (7). Consider the calculation of \mathbf{q}^{n+1} with \mathbf{q}^n assumed to be known. The source term $F(\mathbf{q})$ is decomposed as

$$(27) \quad F(\mathbf{q}) = \mathcal{L}_n(\mathbf{q}) + \mathcal{N}(\mathbf{q}),$$

where \mathcal{L}_n is the Jacobian of F at \mathbf{q}^n

$$(28) \quad \mathcal{L}_n = \text{Jac}_{\mathbf{q}} F(\mathbf{q}^n)$$

The system (26) is rewritten for $t \in [t^n, t^{n+1}]$ as

$$(29) \quad \begin{cases} \frac{d\mathbf{q}(t)}{dt} = \mathcal{L}_n(\mathbf{q}(t)) + \mathcal{N}(\mathbf{q}(t)) \\ \mathbf{q}(t^n) = \mathbf{q}^n \end{cases}$$

³Computational AeroAcoustics

The exact solution of (27) is $\mathbf{q}(t^{n+1})$. It is expressed at time t^{n+1} by

$$(30) \quad \mathbf{q}(t^{n+1}) = \exp(\mathcal{L}_n \Delta t) \mathbf{q}(t^n) + \int_0^{\Delta t} \exp(\mathcal{L}_n(\Delta t - \tau)) \mathcal{N}(\mathbf{q}(t^n + \tau)) d\tau.$$

The integral in the right-hand side of (30) is then approximated but with integrating the exponential "exactly". The function \mathcal{N} is approximated in a Runge-Kutta fashion.

The two following Rosenbrock schemes are used in the sequel:

- The exponentially fitted Euler method is given by

$$(31) \quad \mathbf{q}^{n+1} = \mathbf{q}^n + \Delta t \varphi_1(\Delta t \mathcal{L}_n) F(\mathbf{q}^n),$$

where the function $z \mapsto \varphi_1(z)$ is

$$(32) \quad \varphi_1(z) = (\exp(z) - 1)/z.$$

The scheme (31) is second order in time. It requires one matrix vector product per time iteration.

- The second Rosenbrock time scheme used in Section 4 is

$$(33) \quad \begin{cases} a^n &= \mathbf{q}^n + \Delta t \varphi_1(\Delta t \mathcal{L}_n) F(\mathbf{q}^n), \\ \mathbf{q}^{n+1} &= a^n + 2\Delta t \varphi_3(\Delta t \mathcal{L}_n) (\mathcal{N}(a^n) - \mathcal{N}(\mathbf{q}^n)). \end{cases}$$

The function $\varphi_3(z)$ is

$$(34) \quad \varphi_3(z) = (\exp(z) - 1 - z - z^2/2)/z^3.$$

The scheme (33) is third order in time. Two matrix vector products are required per time step.

For (31) and (33), the filtering step takes place after each time step. In each case, the time stepping has the following form :

Algorithm 2 : Rosenbrock time scheme of order 2 or 3 with filtering step

- 1: $\mathbf{q}^0 = \mathbf{q}^{(0)}$ given,
 - 2: **for** $n = 0, 1, \dots$ itemax **do**
 - 3: Compute $\hat{\mathbf{q}}^{n+1}$ using (31) or (33)
 - 4: Compute $\mathbf{q}^{n+1} = \mathcal{F}(\hat{\mathbf{q}}^{n+1})$.
 - 5: **end for**
-

In the particular case of (1), the linear operator \mathcal{L}_n is given by discretizing the continuous Jacobian of $F(\mathbf{q})$ at the gridfunction $\mathbf{q}^n = [\mathbf{h}^n, \mathbf{u}^n]^T$ with perturbation $\mathbf{q}' = [\mathbf{h}', \mathbf{u}']^T$. It is given by, (see (9) for the notation),

$$(35) \quad \mathcal{L}_n(\mathbf{q}') = - \left[\begin{array}{c} \nabla_{T, \Delta_N} \cdot \left(\{\mathbf{u}^n \bullet \mathbf{h}'\} + \{\mathbf{u}' \bullet (\mathbf{h}^n - h_s(\mathbf{s}))\} \right) \\ \nabla_{T, \Delta_N} (g\mathbf{h}' + \{\mathbf{u}^n \bullet \mathbf{u}'\}) + \left\{ \left(f(\mathbf{s}) + \zeta_{\Delta_N}(\mathbf{s}, \mathbf{u}^n) \right) \bullet (\mathbf{n}(\mathbf{s}) \times \mathbf{u}') \right\} + \left(\left\{ \zeta_{\Delta_N}(\mathbf{s}, \mathbf{u}') \bullet \mathbf{n}(\mathbf{s}) \right\} \times \mathbf{u}^n \right) \right].$$

The function $(\mathbf{s}, \mathbf{u}) \mapsto \zeta_{\Delta_N}(\mathbf{s}, \mathbf{u})$ is given in (11).

Remark 3.2. The operator \mathcal{L}_n in (35) acting on a gridfunction \mathbf{q}' can be equivalently defined as the linearisation at \mathbf{q}^n of the discretisation $F(\mathbf{q})$.

3.3. Krylov method in Rosenbrock schemes. As explained in [28], implementing a Rosenbrock scheme such as (31) or (33) relies on efficiently evaluating matrix vector products of the form $\varphi_l(A)b$ with A the matrix $\Delta t \mathcal{L}_n \Delta t$, and b a vector. The function $z \mapsto \varphi_l(z)$ is a complex function related to the exponential $z \mapsto \exp(z)$. Approximating $\varphi_l(A)b$ is based on the Krylov method.

For $A \in \mathcal{M}_N(\mathbb{R})$ a given matrix and $b \in \mathbb{R}^N$, fix $m \leq N$. The Krylov space $\mathcal{K}_m = \mathcal{K}_m(A, b)$ is the subspace of \mathbb{R}^N defined by

$$(36) \quad \mathcal{K}_m(A, b) = \text{Span} \{b, Ab, A^2b, \dots, A^{m-1}b\}.$$

The integer m is selected as follows, [21, 40]. First m must be picked small enough to efficiently evaluate $\varphi_l(H_m)$. On the other hand it must be large enough to have an accurate approximation of Ab . Typical

values of m are reported in Section 4. Krylov spaces are commonly used to approximate a matrix vector product $f(A)b$ by the Arnoldi method. This idea is the basis for the resolution of large sparse linear systems [32, 33, 42] in the GMRES method. Here the Arnoldi algorithm [32] is used as follows

- Calculate the matrix $H_m \in \mathbb{M}_m(\mathbb{R})$, the projection of A on \mathcal{K}_m . The matrix H_m is expressed as

$$(37) \quad H_m = V_m^T A V_m.$$

where the matrix $V_m \in \mathbb{M}_{N,m}(\mathbb{R})$ has orthonormal columns.

- Approximate A by

$$(38) \quad A \approx V_m H_m V_m^T.$$

- Approximate the vector $\varphi_l(A)b$ by

$$(39) \quad \varphi_l(A)b \approx V_m \varphi_l(H_m) V_m^T b = \|b\|_2 V_m \varphi_l(H_m) e_1$$

where $e_1 \in \mathbb{R}^m$ is the first vector in the canonical basis of \mathbb{R}^m .

The evaluation of $\varphi_l(H_m)$ is obtained by the method in [37]. A rational Padé approximation of $\varphi_l(z)$ is used. In addition, scaling and squaring are used to avoid errors in the case where $\|H_m\| \gg 1$.

4. NUMERICAL RESULTS FOR THE SHALLOW WATER EQUATION

4.1. Introduction. In this section, we report numerical results obtained for (1) using the scheme (7) and either the time scheme RK4 or one of the two Rosenbrock scheme (31) or (33).

Four standard test cases are considered. The three first test cases are the tests 2, 5 and 6 in [45]. They are referred to as the *time-independant geostrophic flow*, the *isolated mountain* and the *Rossby-Haurwitz* case. The fourth test case is the *barotropic instability* in [14]. In all cases, our numerical results are compared to the ones in the literature. The conservation properties of our scheme are numerically evaluated.

The physical constants are $a = 6.37122 \times 10^6 \text{m}$ (earth radius), $\Omega = 7.292 \times 10^{-5} \text{s}^{-1}$ (earth angular velocity), and $g = 9.80616 \text{m} \cdot \text{s}^{-2}$ (gravity constant). The Coriolis force in (2) is given by $f(\mathbf{x}) = 2\Omega \sin \theta$, where θ is the latitude angle. We call I_1 , I_2 and I_3 the following mean values, which are invariants of (1).

$$(40) \quad \left\{ \begin{array}{l} \text{mass : } I_1 = \int_{\mathbb{S}_a^2} (h - h_s) d\mathbf{s}, \\ \text{energy : } I_2 = \int_{\mathbb{S}_a^2} \left(\frac{1}{2} (h - h_s) |\mathbf{u}|^2 + \frac{1}{2} g (h^2 - h_s^2) \right) d\mathbf{s}, \\ \text{potential enstrophy : } I_3 = \int_{\mathbb{S}_a^2} \frac{(\zeta + f)^2}{2(h - h_s)} d\mathbf{s}. \end{array} \right.$$

The numerical error for I_1 , I_2 and I_3 is reported using the relative value

$$(41) \quad \frac{I_p(t) - I_p(0)}{I_p(t)} \text{ for } p = 1, 2, 3.$$

Since the discrete unknown is the gridfunction \mathbf{q}^n , and not discrete averages in cells, the meaning of the discrete version of the averages must be given. All the approximate averages in (40) are calculated using the Cubed Sphere quadrature rule Q_a in [29].

4.2. Time-independent geostrophic flow. Our first test consists in calculating a particular time independent geostrophic flow of (1) (test 2 in [45]). There is no bottom topography i.e. $h_s(\mathbf{x}) = 0$. The Coriolis force is

$$(42) \quad f(\mathbf{x}) = 2\Omega (-\cos \lambda \cos \theta \sin \alpha + \sin \theta \cos \alpha).$$

The angles (λ, θ) are the lon/lat system of coordinates. The parameter angle α is the angle between the zonal axis with the Oz axis. Picking up different values of α permits to evaluate the influence of the position of the

Cubed Sphere with the solution. In our case, it permits to see if there is some interpanel parasitic reflection with our scheme. The exact solution is $q(\mathbf{x}) = [h(\mathbf{x}), \mathbf{u}(\mathbf{x})]^T$, with $\mathbf{u}(\mathbf{x}) = u(\mathbf{x})\mathbf{e}_\lambda(\mathbf{x}) + v(\mathbf{x})\mathbf{e}_\theta(\mathbf{x})$ and

$$(43) \quad \begin{cases} h &= h_0 - \frac{1}{g} \left(a\Omega u_0 + \frac{u_0^2}{2} \right) (-\cos \lambda \cos \theta \sin \alpha + \sin \theta \cos \alpha)^2, \\ u &= u_0 (\cos \theta \cos \alpha + \cos \lambda \sin \theta \sin \alpha), \\ v &= -u_0 \sin \lambda \sin \alpha. \end{cases}$$

The constants h_0 and u_0 are given by $gh_0 = 2.94 \times 10^4 \text{m}^2 \text{s}^{-2}$ and $u_0 = 2\pi a / (12 \text{days})$ (in $\text{m} \cdot \text{s}^{-1}$). Starting from (43) as initial data, the scheme (26) is used, integrated in time by the RK4 scheme. A calculated asymptotic in time state is compared to the initial data. Fig. 2 shows the convergence slope for the relative error $|\mathbf{h} - \mathbf{h}^*|/|\mathbf{h}^*|$ between the steady state \mathbf{h} computed with the RK4 scheme and the exact value $\mathbf{h}^*(\mathbf{s})$ at the grid vertices. Our finest grid is $64 \times 64 \times 6$ with a time step $\Delta t = 300$ seconds, corresponding to $\text{CFL} \simeq 1$ at the equator. The asymptotic state is observed at day 5. This approximately corresponds to 1500 iterations in time. As seen in Fig. 2 both values $\alpha = 0$ and $\alpha = \pi/4$ give a sharp 4-th order accuracy. A very good error level is obtained in both cases. Furthermore, there is no visible influence of the angle α .

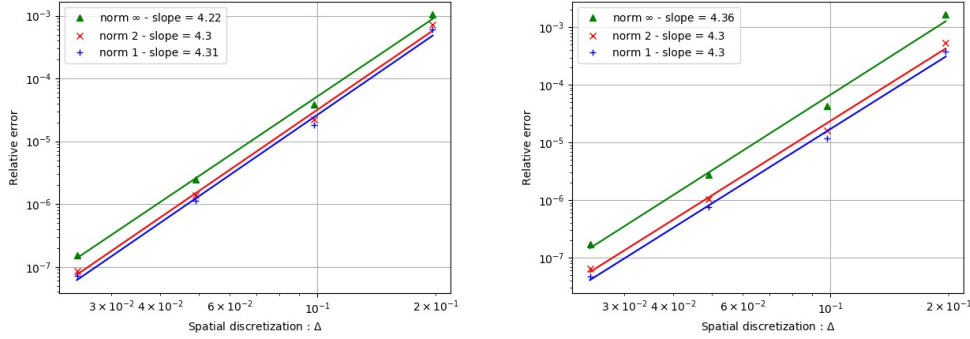


FIGURE 2. Time independent geostrophic flow. The finest grid is $64 \times 64 \times 6$, with a time step corresponding to $\text{CFL} \simeq 1$ at the equator. The numerical solution is computed with the RK4 scheme. It is compared to the exact solution. The convergence slope of the relative error at day 5 in norm 1, 2 and max on the total height h is shown in each case. Left panel: $\alpha = 0$. Right panel: $\alpha = \pi/4$. The $N \times N \times 6$ Cubed Sphere is used with $N = 8, 16, 32$ and 64 . A sharp 4-th order accuracy is observed in both cases. There is no visible influence of the angle α .

4.3. Isolated mountain test case. This is the test 5 in [45]. It is a time dependant case without analytical solution. The initial data is (43) with the parameters $h_0 = 5960 \text{m}$, $u_0 = 20 \text{m} \cdot \text{s}^{-1}$ and $\alpha = 0$. This initial data is perturbed by a conic mountain located at the point (λ_c, θ_c) on \mathbb{S}_a . The bottom topography function $h_s(\mathbf{x})$ is

$$(44) \quad \begin{cases} h_s(\mathbf{x}) = h_{s_0} \left(1 - \frac{r(\mathbf{x})}{r_0} \right), & h_{s_0} = 2000 \text{m}, \\ r = \min \left(r_0, \sqrt{(\lambda - \lambda_c)^2 + (\theta - \theta_c)^2} \right), & r_0 = \pi/9, (\lambda_c, \theta_c) = (3\pi/2, \pi/6). \end{cases}$$

Fig. 3 reports the total height $h(\mathbf{x})$ at day 15. A coarse Cubed Sphere $32 \times 32 \times 6$ is used. The time schemes RK4 and the two Rosenbrock schemes (31) and (33) are used. The isolines are close to those obtained by the conservative schemes in [8, 41]. Fig.4 shows the conservation history for the approximate values I_p , $p = 1 \dots 3$. At day 15, the relative mass conservation is below 10^{-5} in all cases. The mass curve is increasing for the RK4 scheme. It is slightly decreasing with the two Rosenbrock schemes whose curves are superposed. This indicates a good mass conservation property of the spatial approximation. The energy error curves

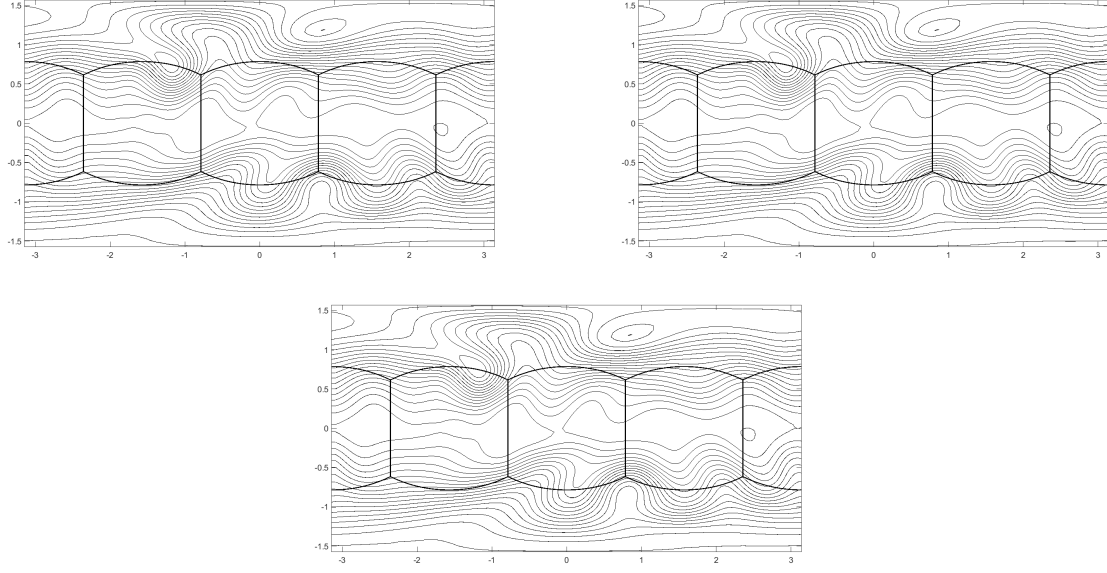


FIGURE 3. Isolated mountain test case at time of 15 days. The total height h is represented. The coarse Cubed Sphere $32 \times 32 \times 6$ is used. The contour line are plotted from 5050m to 5950m with interval of 50m. Top Left : solution using the Rosenbrock time scheme (31). Top Right : Rosenbrock time scheme (33). In both case the time step is $\Delta t = 4h$ ($CFL \simeq 20$). Bottom : solution using RK4 with $\Delta t = 1min$ ($CFL \simeq 0.9$). The results are almost identical.

present a behaviour similar to the mass error curves with the same relative error magnitude. At day 15, the magnitude of the relative error in potential enstrophy is 10^{-5} ($N = 32$) using the Rosenbrock time scheme (31) or (33). The RK4 curve shows a larger dissipation in the enstrophy, reaching a relative error of 10^{-4} . This is the same error level than with a FV scheme [8, 41], the magnitude of this error is 10^{-4} . The curves clearly show that the magnitude of the errors depend on the time scheme. The two Rosenbrock schemes give better conservation results in all cases.

Finally, we report in Table 1 the numerical data used in the Arnoldi method when using the Rosenbrock schemes (31) and (33).

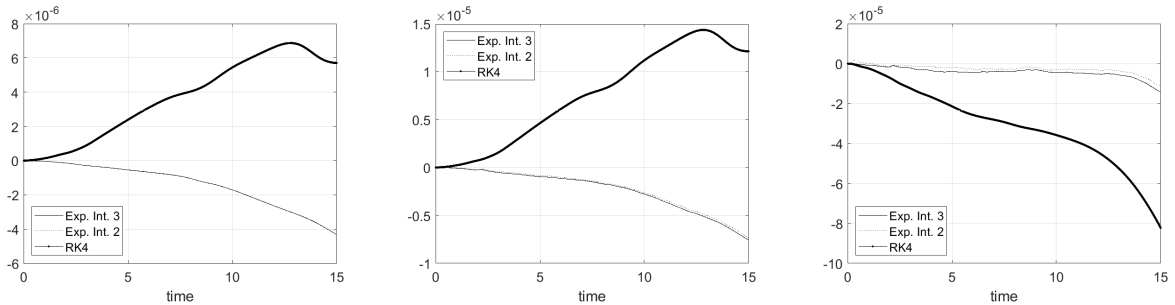


FIGURE 4. Isolated mountain test case with a grid Cubed Sphere $32 \times 32 \times 6$. Conservation error $(I_q(t) - I_q(0))/I_q(0)$. Left panel : mass ($q = 0$). Center panel : energy ($q = 1$). Right panel : potential enstrophy ($q = 2$). Exp. Int. 3 and Exp. Int. 2 correspond to Rosenbrock methods (33) and (31) respectively, both with $\Delta t = 4h$ ($CFL \simeq 20$). The scheme RK4 is considered with $\Delta t = 1min$. ($CFL = 0.9$).

Method	Time step	CFL	number of Krylov vectors
Rosenbrock scheme (31)	$\Delta t = 4\text{h.}$	$\text{CFL} \simeq 20$	52 (for φ_1)
Rosenbrock scheme (33)	$\Delta t = 4\text{h.}$	$\text{CFL} \simeq 20$	52 for φ_1 and 45 (for φ_3)

TABLE 1. Parameters of the two Rosenbrock schemes (31) and (33) for the isolated mountain . The Cubed Sphere is $32 \times 32 \times 6$ (6146 points). The final time is day 15. Maximum number of Krylov vectors used to calculate $\varphi_l(\mathcal{L}_n)b$. The matrix \mathcal{L}_n is full.

4.4. Rossby-Haurwitz test case. The Rossby-Haurwitz is the test 6 in [45]. It is an analytical solution of the nonlinear barotropic vorticity equation [27]. Although this equation is different from the equation (1), it is used to assess the qualitative behaviour of numerical schemes for (1). The initial velocity is $\mathbf{u}(\mathbf{x}) = u(\mathbf{x})\mathbf{e}_\lambda(\mathbf{x}) + v(\mathbf{x})\mathbf{e}_\theta(\mathbf{x})$ with

$$(45) \quad \begin{cases} u(\mathbf{x}) &= a\omega \cos \theta + aK \cos^{R-1} \theta (R \sin^2 \theta - \cos^2 \theta) \cos R\lambda, \\ v(\mathbf{x}) &= -aKR \cos^{R-1} \theta \sin \theta \sin R\lambda. \end{cases}$$

The initial height $h(t=0, \mathbf{x})$ is :

$$(46) \quad gh(t=0, \mathbf{x}) = gh_0 + a^2 A(\theta) + a^2 B(\theta) \cos R\lambda + a^2 C(\theta) \cos 2R\lambda.$$

The functions A , B and C are:

$$(47) \quad \begin{cases} A(\theta) &= \frac{\omega}{2}(2\Omega + \omega) \cos^2 \theta + \frac{1}{4}K^2 \cos^{2R} \theta [(R+1) \cos^2 \theta + (2R^2 - R - 2) - 2R^2 \cos^{-2} \theta], \\ B(\theta) &= \frac{2(\Omega + \omega)K}{(R+1)(R+2)} \cos^R \theta [(R^2 + 2R + 2) - (R+1)^2 \cos^2 \theta], \\ C(\theta) &= \frac{1}{4}K^2 \cos 2R\theta [(R+1) \cos^2 \theta - (R+2)]. \end{cases}$$

The constants are $\omega = K = 7.848 \times 10^{-6} \text{s}^{-1}$, $h_0 = 8 \times 10^3 \text{m}$ and $R = 4$. The function h at day 14 is reported in Fig. 5 with a Cubed Sphere $80 \times 80 \times 6$. The time schemes RK4, and the two Rosenbrock schemes (31) and (33) have been used. For this test, the minimal resolution for accurate results has been found as $80 \times 80 \times 6$. With this grid, the conservation history is reported in Fig. 6 for the first 14 days. The mass conservation is excellent in all cases. As for the isolated mountain, the mass conservation error level is even smaller when using any of the two Rosenbrock schemes (10^{-8}) than with the RK4 scheme (6×10^{-8}). The energy error curves displays an oscillating behaviour for each of the two the Rosenbrock schemes. In all cases, the magnitude of the relative energy error is below 2.5×10^{-6} , which is very good. This is one order of magnitude better than 5×10^{-4} , obtained in [15]. The magnitude of the relative error on the potential enstrophy is 8×10^{-4} compared to 5×10^{-4} obtained in [15]. For the enstrophy, the RK4 scheme and the two Rosenbrock schemes perform similarly. Table 2 reports the numerical data used when using the Rosenbrock schemes (31) and (33).

Method	Time step	CFL	Number of Krylov vectors
Rosenbrock scheme (31)	$\Delta t = 2\text{h.}$	$\text{CFL} \simeq 27$	56 for φ_1
Rosenbrock scheme (33)	$\Delta t = 2\text{h.}$	$\text{CFL} \simeq 27$	56 for φ_1 and 50 for φ_3

TABLE 2. Rossby-Haurwitz case on a Cubed Sphere $80 \times 80 \times 6$ (38402 points). The final time is 14 days. Maximum number of Krylov vectors used to calculate $\varphi_l(\mathcal{L}_n)b$. The matrix \mathcal{L}_n is full.

4.5. Barotropic instability. The last test is the barotropic instability in [14]. The initial condition is $\mathbf{q} = \bar{\mathbf{q}} + \mathbf{q}'$ with the steady state $\bar{\mathbf{q}} = (\bar{h} = h^*, \bar{u} = u^*)$ where (h, \mathbf{u}) is a time independent zonal solution of

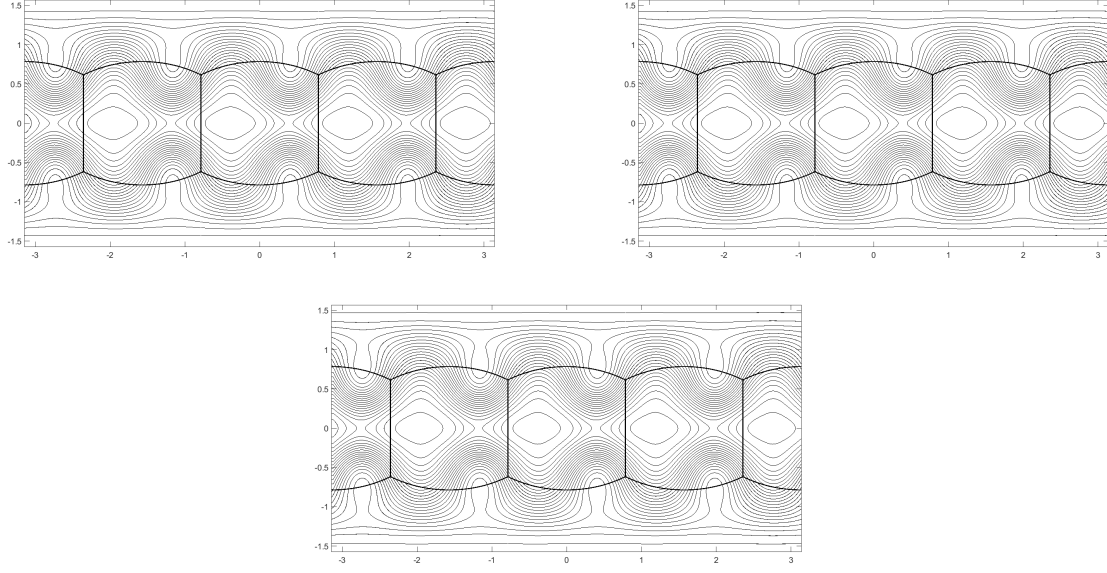


FIGURE 5. Numerical results of the Rossby-Haurwitz test case with the grid $80 \times 80 \times 6$ at day 14. The contour lines are plotted from 8100m to 10500m with interval of 100m. Top Left : Rosenbrock scheme (33). Top Right : Rosenbrock scheme (31). Both with $\Delta t = 2h$. (CFL $\simeq 27$). Bottom : solution using RK4 with $\Delta t = 300sec$. (CFL $\simeq 1$). The differences between the plots are small.

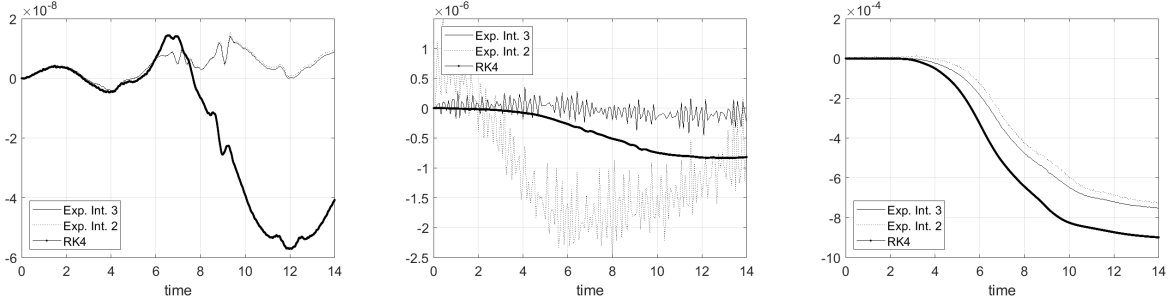


FIGURE 6. Rossby-Haurwitz test case with the grid $80 \times 80 \times 6$. Conservation error $(I_q(t) - I_q(0))/I_q(0)$. Left panel : mass ($q = 0$). Center panel : energy ($q = 1$). Right panel : potential enstrophy ($q = 2$). Exp. Int. 3 and Exp. Int. 2 correspond to Rosenbrock methods (33) and (31) respectively, both with $\Delta t = 2h$ (CFL $\simeq 27$). The scheme RK4 is considered with $\Delta t = 300sec$. (CFL $\simeq 1$). In this case, we remark difference in Rosenbrock scheme contrary to previous case.

(1). The perturbation is $\mathbf{q}'(t = 0) = (h', *, 0)$. The steady state $\bar{\mathbf{q}} = (\bar{h}^*, \bar{\mathbf{u}}^*)$ with \bar{h} and $\bar{\mathbf{u}}$ given by in terms of (λ, θ) by

$$(48) \quad \begin{cases} \bar{h}(\lambda, \theta) &= h_0 - \frac{1}{g} \int_{-\pi/2}^{\theta} a u_{\lambda}(\tau) \left(f + \frac{\tan \tau}{a} u_{\lambda}(\tau) \right) d\tau, \\ \mathbf{u}(\lambda, \theta) &= u_{\lambda}(\theta) \mathbf{e}_{\lambda} \end{cases}$$

with $u_\lambda(\theta) = u_{\max}\psi(\theta)$ and the function $\psi(\theta)$ given by

$$(49) \quad \psi(\theta) = \begin{cases} 0 & \text{if } \theta \leq \theta_0, \\ \frac{1}{e_n} \exp\left(\frac{1}{(\theta - \theta_0)(\theta - \theta_1)}\right) & \text{if } \theta_0 \leq \theta \leq \theta_1, \\ 0 & \text{if } \theta_1 \leq \theta. \end{cases} \quad e_n = \exp\left(\frac{-4}{(\theta - \theta_0)(\theta - \theta_1)}\right)$$

and $(\theta_0, \theta_1) = (\pi/7, \pi/2 - \theta_0)$, $u_{\max} = 80 \text{m} \cdot \text{s}^{-1}$. The height h_0 is such that the mean value of h over the sphere \mathbb{S}_a^2 be 10^4m . The perturbation $h'(\mathbf{x})$ is

$$(50) \quad h'(\lambda, \theta) = \hat{h} \cos \theta \exp \left[- \left(\frac{\lambda}{\alpha} \right)^2 - \left(\frac{\theta_2 - \theta}{\beta} \right)^2 \right],$$

with $\hat{h} = 120 \text{m}$, $\alpha = 1/3$, $\beta = 1/15$ and $\theta_2 = \pi/4$. As mentioned in [38], this test is challenging for a Cubed Sphere discretization since the perturbation is located between the two panels (I) and (V), thus possibly giving some interpanel instability. In addition, the largest magnitude of $\nabla_T h$ is located near panel (V) boundary. In Fig. 7, the contour lines of the vorticity are represented at day 6 for the grid $96 \times 96 \times 6$. The results are similar to those in [8, 41]. As mentioned in [41], the grid $32 \times 32 \times 6$ is too coarse to accurately represent the initial data. The history of the conserved quantities is reported in Fig. 8 with the grid $96 \times 96 \times 6$. Again in all cases, the relative errors are better evaluated with the two Rosenbrock schemes than with the RK4 scheme. For the two Rosenbrock schemes, the relative errors for the mass and for the energy are 10^{-8} and 10^{-6} respectively. As before, the relative potential enstrophy is challenging to preserve. The relative error at day 6 has an order magnitude of 10^{-3} . The numerical parameters when implementing the Rosenbrock schemes (31) and (33) are given in Table 3.

Method	Time step	CFL	Number of Krylov vectors
Rosenbrock scheme (31)	$\Delta t = 1 \text{h}$.	$\text{CFL} \simeq 16$	85 for φ_1
Rosenbrock scheme (33)	$\Delta t = 1 \text{h}$.	$\text{CFL} \simeq 16$	85 for φ_1 and 76 for φ_3

TABLE 3. Barotropic instability case on the Cubed Sphere $96 \times 96 \times 6$, (55298 points). The final time is 6 days. Maximum number of Krylov vectors used to calculate $\varphi_l(\mathcal{L}_n)b$. The matrix \mathcal{L}_n is full.

4.6. General comments on the numerical results. Two conclusions can be drawn from our numerical results. First, the approximation in space shows a very good accuracy. This accuracy is close to 4 as shown in Section 4.2. Furthermore this accuracy is not associated with an interpanel effect of any kind. This is an important property of our spatial approximation. Such an interpanel effect can be present, depending on the type of the Cubed Sphere and on the approximation procedure that are used, [31]. This good behavior is attributed to the Hermitian derivative procedure along the full great circles presented in Section 2. Concerning the stability of the convective term in (1) we never found useful to introduce any upwinding. The mathematical properties of this computational procedure remain to analyze in more detail. Note that an alternative way to interpolate the data of the Cubed Sphere to the set of great circles could be considered. A possibility could be to use some discrete Spherical Harmonics discrete basis associated to the Cubed Sphere. So far however, the cubic spline procedure presented in 2) has been found simple and efficient.

Our second conclusion concerns the Rosenbrock schemes (31) and (33). On the one hand, the numerical results are similar to the ones obtained with the RK4 scheme. However, the relative conservation errors are better with the Rosenbrock schemes than with the RK4 scheme. A much larger CFL number can be used with the Rosenbrock schemes than with the RK4 scheme. This fact is expected, according to the theory of the exponential time schemes [22]. However this is not *per se* an essential issue, since the choice of the time step also depends on the physical phenomena to be simulated. What is found in the present study is that the test cases considered can be run using large time steps. As mentioned in [15], the real issue is to better analyze the computational cost of the Rosenbrock approach using the Krylov procedure in Section 3.3.

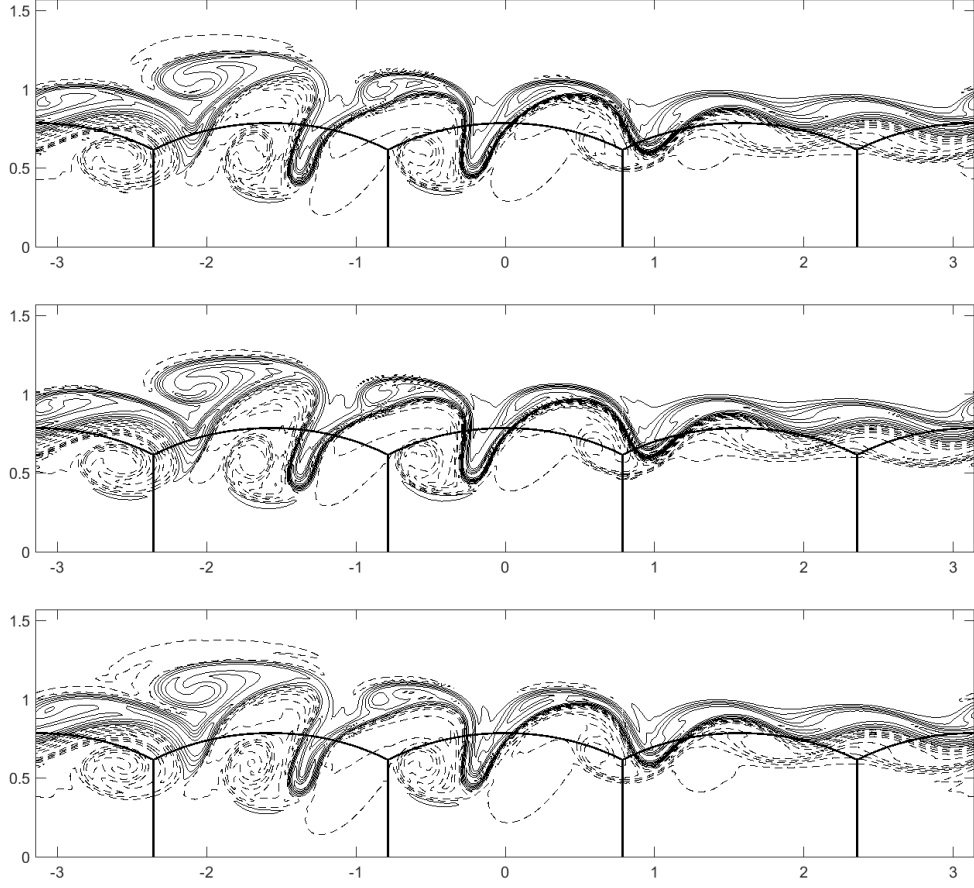


FIGURE 7. Numerical results of the Barotropic instability with the grid $96 \times 96 \times 6$ at day 6. Contour lines of vorticity are plotted. Top : Rosenbrock scheme (33). Center : Rosenbrock scheme (31). Both with $\Delta t = 1\text{h}$ ($\text{CFL} \simeq 16$). Bottom : RK4 scheme with $\Delta t = 240\text{s}$. ($\text{CFL} \simeq 1$). There is no significative differences. Note the absence of interpanel instabilities.

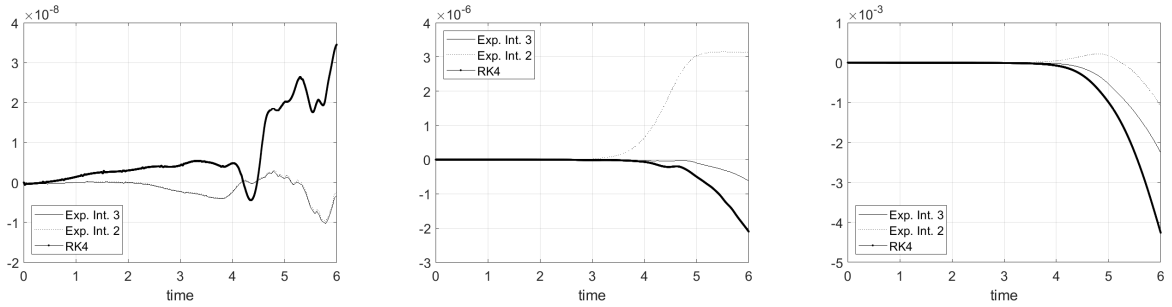


FIGURE 8. Conservation error for the Barotropic instability with the grid $96 \times 96 \times 6$. The conservation error $(I_q(t) - I_q(0))/I_q(0)$. Left panel : mass ($q = 0$). Center panel : energy ($q = 1$). Right panel : potential enstrophy ($q = 2$). Exp. Int. 3 and Exp. Int. 2 correspond to the Rosenbrock schemes (33) and (31) respectively, both with $\Delta t = 1\text{h}$ ($\text{CFL} \simeq 16$). The time step for the RK4 scheme is $\Delta t = 240\text{s}$. ($\text{CFL} \simeq 1$).

5. CONCLUSION

The finite difference approach in GFD simulations was introduced in early works, [34, 1]. Recently, despite of several contributions as [16], this approach has received significantly less attention than the conservative approach stemming from compressible CFD. The present contribution belongs to this category.

The main ideas of the center spatial approximation were introduced in [11, 12] and worked out in [6]. As mentioned in the introduction, this approach is closely related to the standard numerical approach to Computational Aeroacoustics (CAA) by compact schemes. The guiding idea of the present work is that the fluid regime in the test cases presented is closer to the linear regime or to the weakly nonlinear regime than to a strongly nonlinear regime. This makes the GFD flow motion closer from a low Mach number flow than from a shock wave regime. For this reason, centered differencing for the convective term, in a fashion close to the one in CAA, seems a relevant option.

Regarding conservation, the numerical evaluation of integral quantities to be preserved did not reveal any particular misbehaviour with our approach. The numerical results for all the cases tested so far showed sharp fourth order accuracy and very good stability properties. This was found true independently of the particular time stepping scheme used, RK4 or any of the two Rosenbrock schemes considered (31) or (33). These results support the fact that focusing on accuracy in the weakly nonlinear regime is an important challenge for the future of GCM development.

Beyond numerical analysis, many questions remain open. A first question is whether some more nonlinear flow regime in climatology would require more advanced filtering as in [10, 46]. Parallel to this question is which kind of flows in GFD really require upwinding in one form or another.

Another issue is how to efficiently implement the approximation suggested in this paper, as well as how to design some grid refinement procedure. This will be considered in future work. Finally, more complex physical modeling including several layers of shallow water to handle three-dimensional atmospheric flows will be considered as well.

6. APPENDIX: NUMERICAL ANALYSIS

In this section, we gather several numerical analysis facts related to the approximation used in this study. The results are limited to the model problem of the linear convection equation in the periodic setting. Although purely linear and one dimensional, these results were not found in the existing literature.

6.1. Convergence analysis. The approximation in space in Section 2 is based on the standard Hermitian approximate derivative. Consider a regular finite difference grid with stepsize $h > 0$ and periodic data located at point $x_j = jh$, $j = 0, 1, \dots, N-1$. To any gridfunction $\mathbf{w} = [w_0, w_1, \dots, w_{N-1}]$, the Hermitian derivative $\delta_x^H \mathbf{w}$ is defined by

$$(51) \quad \delta_x \mathbf{w}_j - \sigma_x(\delta_x^H \mathbf{w})_j = 0, \quad 0 \leq j \leq N-1,$$

where the operators σ_x and δ_x are defined by

$$(52) \quad \sigma_x \mathbf{v}_j = \frac{1}{6} \mathbf{v}_{j-1} + \frac{2}{3} \mathbf{v}_j + \frac{1}{6} \mathbf{v}_{j+1}, \quad \delta_x \mathbf{v}_j = \frac{\mathbf{v}_{j+1} - \mathbf{v}_{j-1}}{2h}, \quad 0 \leq j \leq N-1.$$

It is well known that $\delta_x^H \mathbf{w}$ is a fourth order approximation to the derivative. It is easily shown that a uniform estimate of the truncation error τ is given by

$$(53) \quad \|\tau\|_\infty \leq \hat{C} h^4 \|\partial_x^{(5)} u^*\|_{\infty, (0, L)}, \quad \hat{C} = 1/60.$$

Next, consider the linear convection equation for the scalar function $u(t, x)$

$$(54) \quad \partial_t u + c \partial_x u = 0, \quad x \in \Omega = (0, L), \quad t \geq 0, \quad c > 0,$$

with periodic conditions at $x = 0$ and $x = L$. The semidiscrete compact scheme is:

$$(55) \quad \frac{d}{dt} \mathbf{v}_j(t) + c \delta_x^H \mathbf{v}_j(t) = 0.$$

This scheme is a standard approximation for convection problems. Refer to [24, 20] and the references therein. Note that the total mass $h \sum_{j=0}^{N-1} \mathbf{v}_j(t)$ is constant in time, which expresses a conservation property of (55).

An elementary convergence analysis, based on the energy method, for the scheme (55) is now carried out as follows. We denote the norm $|\mathbf{u}|_h$

$$(56) \quad |\mathbf{u}|_h = \left(h \sum_{j=0}^{N-1} |u_j|^2 \right)^{1/2}, \quad \|\mathbf{w}\|_{h,\infty} = \max_{0 \leq j \leq N-1} |\mathbf{w}_j|.$$

The error $e_j(t) = u_j^*(t) - \mathbf{v}_j(t)$ evolves along the system

$$(57) \quad \frac{d}{dt} e_j(t) = c \left(\tau_j(t) - \delta_x^H e_j(t) \right), \quad 0 \leq j \leq N-1.$$

Taking the $(\cdot, \cdot)_h$ scalar product of (57) with $e(t)$ gives (the antisymmetry of δ_x^H is used):

$$(58) \quad 2 \left(\frac{d}{dt} e(t), e(t) \right)_h = 2c \left(\tau(t), e(t) \right)_h.$$

Let $\alpha > 0$ be a fixed parameter to be specified latter. The equation (58) implies

$$(59) \quad \frac{d}{dt} |e(t)|_h^2 \leq c \left(\alpha |\tau(t)|_h^2 + \frac{1}{\alpha} |e(t)|_h^2 \right).$$

Applying the Gronwall Lemma easily gives that for t fixed, $e(t)$ satisfies the estimate

$$(60) \quad |e(t)|_h^2 \leq \hat{C}^2 f_{\min} L c^2 t^2 h^8 \|\partial_x^{(5)} u\|_{\infty, [0, T] \times [0, L]}^2, \quad 0 \leq t \leq T.$$

where $f_{\min} = \min_{x>0} (x^2(e^{1/x} - 1))$. Is is easily shown that $f_{\min} \leq 1.545$. Defining the constant $\tilde{C} = \hat{C} \sqrt{f_{\min}} \simeq 2.08 \cdot 10^{-2}$, we obtain finally the following

Proposition 6.1. Let $u_j^* = u(t, x)$ be the exact solution of (54) at points x_j and $\mathbf{v}_j(t)$ be the solution of semidiscrete scheme (55). The error $e_j(t) = u^*(t) - \mathbf{v}_j(t)$ satisfies the fourth order error estimate

$$(61) \quad |e_j(t)|_h \leq C(t) h^4 \|\partial_x^{(5)} u\|_{\infty, [0, T] \times [0, L]}, \quad 0 \leq t \leq T,$$

where $C(t) = \tilde{C} \sqrt{L} c t$ and $\tilde{C} \simeq 2.08 \cdot 10^{-2}$ is a universal constant.

The estimate (61) shows a linear evolution of the constant $C(t)$ in time from $t = 0$ to $t = T$.

Remark 6.2. The estimate (61) shows fourth order accuracy in the grid dependent norm $|\cdot|_h$. Note that the maximum norm estimate is more difficult to prove. Note also that the practical interest of Prop. 6.1 is limited to the constant velocity and regular grid cases.

6.2. Matrix stability analysis of the fully discrete scheme. In this section, we show how to derive analytically the matrix stability condition for (55) when discretized in time by the RK4 scheme. Let $V(t) = [v_0(t), v_1(t), \dots, v_{N-1}(t)]^T$. The equation (55) is equivalent to the vector equation

$$(62) \quad \begin{cases} \frac{d}{dt} V(t) = -\frac{c}{h} \mathbf{J} V(t), \\ V(0) = V_0 = [u_0^*, u_1^*, \dots, u_{N-1}^*]^T, \end{cases}$$

where \mathbf{J} is the $N \times N$ matrix defined by $(\mathbf{J}V)_j = \delta_x^H \mathbf{v}_j$. Let \mathbf{P} be the matrix of the left shift operator $u_j \mapsto u_{j-1}$ with N -periodic data.

$$(63) \quad \mathbf{P} = \underbrace{\begin{bmatrix} 0 & 1 & & & \\ & 0 & 1 & (0) & \\ & & \ddots & \ddots & \\ (0) & & & 0 & 1 \\ 1 & & & & 0 \end{bmatrix}}_{N \times N}.$$

The matrix \mathbf{J} is $\mathbf{J} = m(\mathbf{P})$ where

$$(64) \quad m(z) = \frac{1}{2} \frac{z - z^{-1}}{\frac{1}{6}(z + z^{-1}) + \frac{2}{3}}.$$

The matrices \mathbf{P} and \mathbf{J} are expressed as ⁴

$$(65) \quad \mathbf{P} = \sum_{k=-\frac{N}{2}+1}^{\frac{N}{2}} \omega^k R^k \otimes (R^k)^H,$$

and

$$(66) \quad \mathbf{J} = \sum_{k=-\frac{N}{2}+1}^{\frac{N}{2}} m(\omega^k) R^k \otimes (R^k)^H.$$

where $R^k = [R_0^k, R_1^k, \dots, R_{N-1}^k]^T \in \mathbb{C}^N$ is the vector with components

$$(67) \quad R_j^k = \frac{1}{\sqrt{N}} \omega^{kj}, \quad 0 \leq j \leq N-1, \quad \omega = \exp\left(\frac{2i\pi}{N}\right).$$

Using that $V(t) = \exp(-\frac{ct}{h}\mathbf{J})V_0$ yields

$$(68) \quad V(t) = \sum_{k=-\frac{N}{2}+1}^{\frac{N}{2}} \exp\left(-\frac{c}{h}m(\omega^k)t\right) ((R^k)^H V_0) R^k.$$

Consider now the time stepping of (62) by the RK4 scheme, [44, Chap. IV.2, pp. 16-18]. Since the matrix $-c\mathbf{J}/h$ is constant, the RK4 time stepping coincides with the vector iteration

$$(69) \quad V^{n+1} = r(-\lambda\mathbf{J})V^n,$$

where $\lambda = c\Delta t/h > 0$ is the Courant number and $r(z)$ is the truncated exponential series

$$(70) \quad r(z) = 1 + z + \frac{z^2}{2!} + \frac{z^3}{3!} + \frac{z^4}{4!}.$$

Using (66) gives that V^n is

$$(71) \quad V^n = \sum_{k=-\frac{N}{2}+1}^{\frac{N}{2}} [r(-\lambda m(\omega^k))]^n ((R^k)^H V_0) R^k.$$

The sequence (71) is bounded if and only if

$$(72) \quad \max_{k=-N/2+1}^{N/2} |r(-\lambda m(\omega^k))| \leq 1.$$

This is equivalent to

$$(73) \quad \lambda \max_{k=-N/2+1}^{N/2} |m(\omega_k)| \leq K_{\text{RK4}},$$

where $K_{\text{RK4}} = 2\sqrt{2}$ is defined by

$$(74) \quad K_{\text{RK4}} = \max\{b, \text{ where } a + ib \in \mathcal{D}_{\text{RK4}}\} = 2\sqrt{2}.$$

where \mathcal{D}_{RK4} is the domain of stability of the RK4 scheme, [44, Chap. IV.2, p. 18]. The condition (73) is rewritten as

$$(75) \quad \lambda \max_{k=-N/2+1}^{N/2} \left(\frac{\sin\left(\frac{2k\pi}{N}\right)}{\frac{2}{3} + \frac{1}{3} \cos\left(\frac{2k\pi}{N}\right)} \right) \leq K_{\text{RK4}},$$

or equivalently

$$(76) \quad \lambda \leq 2\sqrt{2/3}.$$

We have proved the matrix stability analysis result:

⁴For X a $n \times m$ matrix, $X^H = \bar{X}^T$

Proposition 6.3. The sequence $(V^n)_{n \geq 0}$ is uniformly bounded under the necessary and sufficient condition

$$(77) \quad \lambda \leq \lambda_\infty, \text{ where } \lambda_\infty = 2\sqrt{2/3}.$$

6.3. Filtered time-scheme. The preceding stability condition is an indication for a bound of the CFL. However it is only valid for the linear equation (54). In the case of a non constant velocity model, the stability must be reinforced. This is of course not surprizing, since the basic scheme is centered. A common treatment consists in adding at each time step a high-frequency filter. Refer to [5] and references therein. This filtering step takes the form (see the last line in Algorithm 1 in Section 3.1):

$$(78) \quad V^{n+1} = \mathcal{F} \left(V^n + \frac{\Delta t}{6} \left(K^{(0)} + 2K^{(1)} + 2K^{(2)} + K^{(3)} \right) \right),$$

or equivalently

$$(79) \quad V^{n+1} = \mathcal{F} (r (-\lambda \mathbf{J}) V^n).$$

The filter function \mathcal{F} is the linear operator acting on periodic sequences defined by

$$(80) \quad \mathcal{F}(u_i)_i = \sum_{j=0}^J \frac{a_j}{2} (u_{i+j} + u_{i-j}), \quad 0 \leq j \leq N-1.$$

The width of the stencil is the odd integer $2J+1$. The first $J+1$ coefficients a_0, a_1, \dots, a_J must satisfy the $J+1$ equations

$$(81) \quad \begin{cases} \sum_{j=0}^J a_j = 1, & (a)_0 \\ \sum_{j=0}^J a_j j^{2k} = 0, & k = 1 \dots J-1, \quad (a)_k \\ \sum_{j=0}^J a_j (-1)^j = 0, & (b) \end{cases}$$

The $J+1$ equations $(a)_k$, with $k = 0, 1, \dots, J-1$ translate the consistency with the identity of the filter

Order of accuracy	a_0	a_1	a_2	a_3	a_4	a_5
2	1/2	1/2				
4	10/16	8/16	-2/16			
6	44/64	30/64	-12/64	2/64		
8	186/256	112/256	-56/256	16/256	-2/256	
10	772/1024	420/1024	-240/1024	90/1024	-20/1024	2/1024

TABLE 4. Examples of filters in the form (80) and their orders of accuracy.

function with accuracy $2J$. These relations are obtained by Taylor expansions near x_i . The additional relation $(81)_b$ translates that the oscillating mode $\mathbf{v}_j = (-1)^j$ is cancelled out by the operator \mathcal{F} . The linear system (81) is (we drop the dependence in J for simplicity)

$$(82) \quad \mathbf{A} \mathbf{a} = \mathbf{b},$$

Accuracy of \mathcal{F} , $2J$	λ_J
∞ (no filter)	1.6329
10	1.6883
8	1.7114
6	1.7485
4	1.8156
2	1.9749

TABLE 5. Maximum CFL number λ_J for the vector iteration (79) in term of J , the width of the stencil of the filter function \mathcal{F} . The function $J \mapsto \lambda_J$ is decreasing. The limit value is $\lambda_\infty = 2\sqrt{2/3} \simeq 1.6239$. This limit value corresponds to $J = +\infty$, i.e. the absence of filtering.

where the $\mathbf{a} = [a_0, a_1, \dots, a_J]^T$ is the vector of coefficients in (80), $\mathbf{b} = [1, 0, \dots, 0]^T \in \mathbb{R}^{J+1}$ and \mathbf{A} is the $(J+1) \times (J+1)$ matrix

$$(83) \quad \mathbf{A} = \begin{pmatrix} 1 & 1 & 1 & 1 & 1 & 1 & \cdots \\ 0 & 2 & 0 & 2 & 0 & 2 & \cdots \\ 0 & 1 & 2^2 & 3^2 & 4^2 & 5^2 & \cdots \\ 0 & 1 & 2^4 & 3^4 & 4^4 & 5^4 & \cdots \\ 0 & 1 & 2^6 & 3^6 & 4^6 & 5^6 & \cdots \\ & & & \vdots & \vdots & & \end{pmatrix}.$$

We skip the proof of the following proposition, which states existence and uniqueness of the coefficients \mathbf{a} :

Proposition 6.4. There exists a unique set $[a_0, a_1, \dots, a_J]$ satisfying the relations (81). The filter function \mathcal{F} in (80) operates on each periodic gridfunction R^k by

$$(84) \quad \mathcal{F}(R^k)_j = P_J(\cos(\theta))R_j^k,$$

where P_J is the polynomial

$$(85) \quad P_J(X) = 1 - \frac{1}{2^J}(1 - X)^J.$$

Moreover, for all periodic gridfunction $(\mathbf{w}_j)_{0 \leq j \leq N-1}$

$$(86) \quad \max_{0 \leq j \leq N-1} |\mathcal{F}(\mathbf{w})_j| \leq \max_{0 \leq j \leq N-1} |w_j|,$$

and the stability condition of the iteration (78) is $\lambda \leq \lambda_J$ where $\lambda_J \geq \lambda_\infty$.

Table 4 reports the values of a series of filter coefficients \mathbf{a}_J [43]. In addition, a set of approximate values of λ_J is reported in Table 5. As expected, the lower J , the higher the maximal CFL number λ_J .

REFERENCES

- [1] A. Arakawa. Computational design for long-term numerical integration of the equations of fluid motion: Two-dimensional incompressible flow. Part I. *J. Comput. Phys.*, 1(1):119–143, 1966.
- [2] L. Bao, R. D. Nair, and H. M. Tufo. A mass and momentum flux-form high-order discontinuous Galerkin shallow water model on the Cubed-Sphere. *J. Comput. Phys.*, 271:224–243, 2014.
- [3] M. Ben-Artzi, J.-P. Croisille, and D. Fishelov. *Navier-Stokes equations in planar domains*. Imp. Coll. Press, 2011.
- [4] M. Ben-Artzi, J. Falcovitz, and P. G. LeFloch. Hyperbolic conservation laws on the sphere. A geometry-compatible finite volume scheme. *J. Comput. Phys.*, 228(16):5650–5668, 2009.
- [5] C. Bogey and C. Bailly. A family of low dispersive and low dissipative explicit schemes for flow and noise computations. *J. Comput. Phys.*, 194(1):194–214, 2004.
- [6] M. Brachet. *Schémas compacts hermitiens sur la Sphère: applications en climatologie et océanographie numérique*. PhD thesis, Univ. de Lorraine, 2018.
- [7] C. Jablonowski and P. Lauritzen and R. D. Nair and M. Taylor. Idealized test cases for the dynamical cores of atmospheric general circulation models. A proposal for the NCAR ASP 2008 summer colloquium, 2008.

- [8] C. Chen and F. Xiao. Shallow water model on cubed-sphere by multi-moment finite volume method. *J. Comput. Phys.*, 227(10):5019–5044, 2008.
- [9] C. Clancy and J. A. Pudykiewicz. On the use of exponential time integration methods in atmospheric models. *Tellus A*, 65(1):20898, 2013.
- [10] A. W. Cook and W. H. Cabot. Hyperviscosity for shock-turbulence interactions. *J. Comput. Phys.*, 203(2):379–385, 2005.
- [11] J.-P. Croisille. Hermitian compact interpolation on the cubed-sphere grid. *J. Sci. Comput.*, 57(1):193–212, 2013.
- [12] J.-P. Croisille. Hermitian approximation of the spherical divergence on the Cubed-Sphere. *Jour. Comp. App. Math.*, 280:188–201, 2015.
- [13] C. Eldred and D. Randall. Total energy and potential enstrophy conserving schemes for the shallow water equations using Hamiltonian methods—Part 1: Derivation and properties. *Geosci. Model Dev.*, 10(2):791–810, 2017.
- [14] J. Galewski, R. K. Scott, and L. M. Polvani. An initial-value problem for testing numerical models of the global shallow-water equations. *Tellus A*, 56(5):429–440, 2004.
- [15] S. Gaudreault and J. A. Pudykiewicz. An efficient exponential time integration method for the numerical solution of the shallow water equations on the sphere. *J. Comput. Phys.*, 322:827–848, 2016.
- [16] S. Ghader and J. Nordström. High-order compact finite difference schemes for the vorticity–divergence representation of the spherical shallow water equations. *Int. J. Numer. Methods Fluids*, 78(12):709–738, 2015.
- [17] M. Ghil and S. Childress. *Topics in geophysical fluid dynamics: atmospheric dynamics, dynamo theory, and climate dynamics*, volume 60. Springer Science & Business Media, 1987.
- [18] F. X. Giraldo. A spectral element shallow water model on spherical geodesic grids. *Int. J. Numer. Meth. Fluids*, 35(8):869–901, 2001.
- [19] O. Guba, M. Taylor, and A. St-Cyr. Optimization-based limiters for the spectral element method. *J. Comput. Phys.*, 267:176–195, 2014.
- [20] B. Gustafsson. *High Order Difference Methods for Time Dependent PDE*. Springer-Verlag, 2008.
- [21] M. Hochbruck and C. Lubich. On Krylov subspace approximations to the matrix exponential operator. *SIAM J. Num. Anal.*, 34(5):1911–1925, 1997.
- [22] M. Hochbruck and A. Ostermann. Exponential integrators. *Acta Numerica*, 19:209–286, 2010.
- [23] R. Jakob-Chien, J. J. Hack, and D. L. Williamson. Spectral transform solutions to the shallow water test set. *J. Comput. Phys.*, 119(1):164–187, 1995.
- [24] S. K. Lele. Compact Finite Difference Schemes with Spectral-like Resolution. *J. Comput. Phys.*, 103, 1991.
- [25] R. D. Nair, H.-W. Choi, and H. M. Tufo. Computational aspects of a scalable high-order discontinuous Galerkin atmospheric dynamical core. *Comput. & Fluids*, 38(2):309–319, 2009.
- [26] N. Paldor. *Shallow water waves on the rotating Earth*. Springer, 2015.
- [27] J. Pedlosky. *Geophysical fluid dynamics*. Springer Science & Business Media, 1987.
- [28] K. Pieper, K. C. Sockwell, and M. Gunzburger. Exponential time differencing for mimetic multilayer ocean models. *arXiv preprint arXiv:1901.08116*, 2019.
- [29] B. Portelenelle and J.-P. Croisille. An efficient quadrature rule on the Cubed Sphere. *Jour. Comp. App. Math.*, 328:59–74, 2018.
- [30] R.J. Purser and M. Rancic. Smooth quasi-homogeneous gridding of the sphere. *J. Comput. Phys.*, 124:637–647, 1998.
- [31] W.M. Putman and S.-J. Lin. Finite volume transport on various cubed-sphere grids. *J. Comput. Phys.*, 227:55–78, 2007.
- [32] Y. Saad. *Iterative methods for sparse linear systems*, volume 82. SIAM, 2003.
- [33] Y. Saad and M. H. Schultz. GMRES: A generalized minimal residual algorithm for solving nonsymmetric linear systems. *SIAM J. Sci. Stat. Comput.*, 7(3):856–869, 1986.
- [34] R. Sadourny. Conservative finite-difference approximations of the Primitive equations on Quasi-Uniform spherical grid. *Mon. Wea. Rev.*, 100 (2), 1972.
- [35] J. Shipton, T. H. Gibson, and C. J. Cotter. Higher-order compatible finite element schemes for the nonlinear rotating shallow water equations on the sphere. *J. Comput. Phys.*, 375:1121–1137, 2018.
- [36] J. G. Simmonds. *A Brief on Tensor Analysis*. Undergraduate Texts in Math. Springer, 2cd edition, 1994.
- [37] B. Skaflestad and W. M. Wright. The scaling and modified squaring method for matrix functions related to the exponential. *App. Num. Math.*, 59(3-4):783–799, 2009.
- [38] A. St-Cyr, C. Jablonowski, J. M. Dennis, H. M. Tufo, and S. J. Thomas. A comparison of two shallow-water models with nonconforming adaptive grids. *Mon. Wea. Rev.*, 136(6):1898–1922, 2008.
- [39] J. Thuburn, C.J. Cotter, and T. Dubos. A Mimetic, semi-implicit, forward-in-time, finite volume shallow water model: comparison of hexagonal-icosahedral and Cubed-Sphere grids. *Geosci. Model Dev.*, 7(3):909–929, 2014.
- [40] M. Tokman. Efficient integration of large stiff systems of ODEs with exponential propagation iterative (EPI) methods. *J. Comput. Phys.*, 213(2):748–776, 2006.
- [41] P. A. Ullrich, C. Jablonowski, and B. Van Leer. High-order finite-volume methods for the shallow-water equations on the sphere. *J. Comput. Phys.*, 229(17):6104–6134, 2010.
- [42] H. A. Van der Vorst. An iterative solution method for solving $f(A)X = b$, using Krylov subspace information obtained for the symmetric positive definite matrix A . *J. Comput. App. Math.*, 18(2):249–263, 1987.
- [43] M. R. Visbal and D. V. Gaitonde. On the use of higher-order finite-difference schemes on curvilinear and deforming meshes. *J. Comput. Phys.*, 181(1):155–185, 2002.
- [44] G. Wanner and E. Hairer. *Solving ordinary differential equations II*. Springer Berlin Heidelberg, 1996.

- [45] D. L. Williamson, J. B. Drake, J. J. Hack, R. Jakob, and P. N. Swarztrauber. A standard test set for numerical approximations to the shallow water equations in spherical geometry. *J. Comput. Phys.*, 102(1):211–224, 1992.
- [46] H. C. Yee and B. Sjögren. Designing adaptive low-dissipative high order schemes for long-time integrations. In *Turb. Flow Comput.*, pages 141–198. Springer, 2004.

‡UNIVERSITÉ DE LORRAINE, DÉPARTEMENT DE MATHÉMATIQUES, F-57045 METZ, FRANCE,, †INRIA, GRENOBLE, FRANCE,
‡C.N.R.S., INSTITUT ELIE CARTAN DE LORRAINE, UMR 7502, F-57045 METZ, FRANCE
E-mail address: †matthieu.brachet@inria.fr, ‡jean-pierre.croisille@univ-lorraine.fr